WATER RESOURCES RESEARCH, VOL. 49, 8480–8494, doi:10.1002/2013WR013992, 2013

Coupled hydrogeophysical inversion of time-lapse surface GPR data to estimate hydraulic properties of a layered subsurface

Sebastian Busch,[1] Lutz Weihermüller,[1] Johan A. Huisman,[1] Colby M. Steelman,[2] Anthony L. Endres,[3]
Harry Vereecken,[1] and Jan van der Kruk[1]

Received 19 April 2013; revised 21 November 2013; accepted 26 November 2013; published 17 December 2013.

[1] A major challenge in vadose zone hydrology is to obtain accurate information on the temporal changes of the vertical soil water distribution and its feedback with the atmosphere and groundwater. A state of the art coupled hydrogeophysical inversion scheme is applied to evaluate soil hydraulic properties of a synthetic model and a field soil in southern Ontario based on time-lapse monitoring of soil dynamics with surface ground-penetrating radar (GPR). Film flow was included in the hydrological model to account for noncapillary water flow in a sandy medium during dry conditions. The synthetic study illustrated that GPR data contain sufficient information to accurately constrain soil hydraulic parameters within a coupled inversion framework and led to an accurate estimation of the soil hydraulic properties. When film flow was not accounted for within the inversion, an equally good fit could still be achieved. In this case, errors introduced by neglecting film flow were compensated by different hydraulic parameters. For the field data, the coupled inversion reduced the overall misfit compared to an uncalibrated model using hydraulic parameters obtained from laboratory data. Although the data fit improved significantly for water content in the deeper soil layers, accounting for film flow in the uppermost subsurface layer did not lead to a better fit of the GPR data. Further research is needed to describe the processes controlling water content in the dry range, in particular coupled heat and vapor transport. This study illustrates the suitability of surface GPR measurements combined with coupled inversion for near-surface characterization of soil hydraulic parameters.

Citation: Busch, S., L. Weihermüller, J. A. Huisman, C. M. Steelman, A. L. Endres, H. Vereecken, and J. van der Kruk (2013), Coupled hydrogeophysical inversion of time-lapse surface GPR data to estimate hydraulic properties of a layered subsurface, *Water Resour. Res.*, *49*, 8480–8494, doi:10.1002/2013WR013992.

1. Introduction

[2] Understanding highly dynamic hydrological processes in the subsurface is an important and challenging task for many applications ranging from agriculture and soil sciences to hydrology and meteorology. Obtaining accurate estimates of soil hydraulic properties is essential for the prediction of water flow through the system and its interaction with the atmosphere and ground water, respectively, and are required to simulate these processes. Nevertheless, modeling of hydrological processes is not straightforward due to the highly dynamical nature of processes such as evaporation and precipitation and the spatial variability of the soil hydraulic properties [*Ersahin and Brohi*, 2006; *Behaegel et al*., 2007] which also limits the understanding of the system.

[3] Promising techniques to characterize dynamic processes in the subsurface are time-lapse geophysical surveys in combination with coupled inversion schemes where a hydrological model of the subsurface is combined with a geophysical forward model. Recently, *Hinnell et al*. [2010] described the advantages and assumptions of the coupled inversion approach in detail. Compared to conventionally used sequential inversion approaches where the measured geophysical data and the hydrological model are inverted independently, the error propagation from the data inversion to the hydrological model inversion is minimized [e.g., *Hinnell et al*., 2010; *Mboh et al*., 2011].

[4] Ground-penetrating radar (GPR) techniques are promising for characterizing soil moisture dynamics [*Huisman et al*., 2003]. Similar to the well-established time domain reflectometry (TDR) method, GPR techniques are based on electromagnetic (EM) wave propagation and their larger sampling volume is much better suited for field-scale applications. Cross-borehole GPR has been successfully used in a number of studies to estimate soil hydraulic

---

[1] Institute of Bio- and Geosciences: Agrosphere (IBG-3), Forschungszentrum Jülich, Jülich, Germany.

[2] School of Engineering, University of Guelph, Guelph, Ontario, Canada.

[3] Department of Earth and Environmental Sciences, University of Waterloo, Waterloo, Ontario, Canada.

Corresponding author: S. Busch, Institute of Bio- and Geosciences: Agrosphere (IBG-3), Forschungszentrum Jülich, 52428 Jülich, Germany. (s.busch@fz-juelich.de)

0043-1397/13/10.1002/2013WR013992

properties using coupled inversion schemes [*Rucker and Ferré*, 2004; *Kowalsky et al*., 2005; *Looms et al*., 2008], but is restricted by the need for appropriate borehole installations. *Lambot et al*. [2004, 2006a, 2009] have developed a coupled inversion scheme to estimate soil hydraulic properties of the shallow subsurface using off-ground (i.e., air launched) GPR data. Recently, *Jadoon et al*. [2012] used a coupled inversion approach to calibrate a two-layer hydrologic model of an agricultural field, which was conceptualized by a plow horizon (0–32 cm) with a spatially uniform thickness and a homogeneous underlying layer (32–60 cm). Although the work of *Jadoon et al*. [2012] represents a promising application of coupled inversion schemes, one of the main challenges using off-ground GPR is its sensitivity to surface roughness [*Lambot et al*., 2006b] and the limited penetration depth of the GPR signal.

[5] Given the noninvasive nature and potential depth of investigation, surface GPR methods such as reflection profiling and common midpoint (CMP) sounding are promising for obtaining hydrological information. However, there are only a few studies focusing on inversion of surface GPR field data for hydrological parameter estimation. For example, *Moysey* [2010] presents a sandbox infiltration experiment combined with HYDRUS-1D to demonstrate how GPR reflection data enable the estimation of the soil hydraulic properties. The author shows that infiltration and redistribution of water in a homogeneous soil produce distinctive patterns in a constant offset GPR data caused by travel time shifts of different GPR arrivals as soil moisture conditions change. These patterns result in coherent signals that appear to follow hydrologically defined trajectories through time which is analogous to normal-moveout trajectories used in the semblance velocity analysis. Recently, *Steelman et al*. [2012] conducted an extensive field study covering two contrasting annual cycles of soil conditions typical of midlatitude climates. In that study, GPR reflection profiling and CMP soundings were carried out in a daily to weekly interval to characterize vertical soil water dynamics within the vadose zone. This unique data set illustrated the highly variable nature of soil water content in the upper 3 m over both seasonal and shorter time scales. To examine the potential information content of their GPR-derived soil water profiles for estimating hydraulic parameters, *Steelman et al*. [2012] compared their GPR observations with soil water flow simulations using a one-dimensional hydrological model (HYDRUS-1D) parameterized with laboratory-derived Brooks-Corey (BC) soil hydraulic properties [*Brooks and Corey*, 1966] obtained from repacked soil samples. Here the simulated and measured results of *Steelman et al*. [2012] matched fairly well and the authors hypothesized that the good fit between their uncalibrated modeling results and GPR-derived soil moisture estimates provided strong evidence that surface GPR data can be used for soil hydraulic parameter estimation.

[6] The aim of this study is to extend the analysis of *Steelman et al*. [2012] and assess the feasibility of estimating soil hydraulic properties of a layered subsurface using a coupled inversion scheme applied to surface GPR data, where measured interval travel times are combined with a hydrological model of the subsurface. First, a synthetic surface GPR data set is used to determine whether surface GPR measurements contain sufficient information for the estimation of soil hydraulic properties of a multilayered medium. Afterward, our coupled inversion approach is applied to the data set of *Steelman et al*. [2012] to examine its performance when applied to real field data.

2. Methodology

[7] Although water content can be directly calculated from GPR velocity analysis using petrophysical and empirical relationships, such as the Complex Refractive Index Model (CRIM; *Wharton et al*. [1980]) and Topp's equation [*Topp et al*., 1980], the estimation of soil hydraulic properties is not feasible if the movement of water over time and depth is unknown. Here we use time-lapse common midpoint (CMP) GPR data measured on an agricultural test site to obtain in situ travel times and interval velocities that reflect water content changes in the upper few meters of the vadose zone, enabling the estimation of unsaturated soil hydraulic properties over discrete depth intervals. A hydrological model with input from a nearby weather station was used to generate water content distribution dynamics that are converted to GPR travel times and interval velocities using the CRIM model at those dates when the GPR data were measured. The misfit between the simulated and observed GPR interval travel times was minimized by updating the parameters of the hydrological model using the shuffled complex evolution approach (SCE-UA) as described by *Duan et al*. [1992]. The SCE-UA is a fast and robust optimization routine which is well suited to solve inherently ill-posed inverse problems with a large number of unknown parameters. The SCE-UA algorithm has been already successfully used in various applications ranging from vadose zone model parameterization [e.g., *Mertens et al*., 2005] to the estimation of parameters in nonlinear carbon models [e.g., *Weihermüller et al*., 2009; *Bauer et al*., 2012] and coupled hydrogeophysical inversions [e.g., *Mboh et al*., 2011].

[8] The GPR data used in this study were initially analyzed by *Steelman et al*. [2012] and a brief summary of the field methodology and interpretation of the results needed for the current analysis is provided below.

2.1. Test Site

[9] The monitoring transect of the time-lapse GPR measurements was positioned on top of a local sandy hill characterized by interbedded fine to coarse sand. GPR common-offset profiling and CMP soundings were carried out in a daily to weekly interval [*Steelman et al*., 2012]. Based on nearby water bodies and supporting geophysical measurements, the local water table is expected at a depth of 15–20 m below the ground surface. During the study period, no agricultural management operations such as plowing and tillage were performed on the test site.

[10] Detailed soil physical properties of the study site were obtained from soil samples down to a depth of 1.6 m, which were extracted at the end of the experiment on a fresh trench wall. The exposed vertical section of the soil was characterized by a 0.25 m dark colored plow horizon composed of coarse sand containing approximately 1.5% (wt/wt) organic material and 3% (wt/wt) silt fraction overlying clean, well-sorted sequences of fine to coarse grained

sand layers with a thickness ranging from centimeters to decimeters.

2.2. Interval Velocity and Depth Model Estimation From GPR Data

[11] To determine interval velocity and layer depth from the GPR survey (see Figure 1), a layered subsurface was assumed and suitable reflections in CMP data were identified using the following criteria: (i) reflections are laterally continuous with consistent vertical separation across the monitoring profile, (ii) reflections correspond to major stratigraphic boundaries, and (iii) reflections are clearly identifiable in both the reflection and CMP data. Figure 1a shows a characteristic GPR CMP data set that clearly shows four reflections coming from the major stratigraphic boundaries present at the test site and Figure 1b indicates the associated ray paths.

[12] Conventional normal-moveout (NMO) velocity and travel time analyses of the reflected waves were carried out by *Steelman* [2012] and *Steelman et al.* [2012], who also discussed the challenges in obtaining the NMO velocity (v^{NMO}) for time-lapse surface GPR measurements. The calculated v^{NMO} indicate long-term temporal patterns that follow general seasonal moisture trends such that lower v^{NMO} encountered during wetter spring and autumn periods while higher v^{NMO} were observed during dryer summer and frozen winter conditions [*Steelman*, 2012]. For each CMP data set, the semblance velocity spectrum was calculated and the "first break" of the GPR wavelet was picked to extract the velocity information [*Steelman et al.*, 2012]. The results of the NMO analysis were then used to calculate an average layer thickness for all data sets. Using an average layer depth and calculating the two-way travel time to each reflector present in the measured CMP data returned the interval travel time and the interval velocities (Figure 1b).

[13] Since the intervals are assumed to represent stratigraphic boundaries, the layer thickness is fixed to the known layer depths in the remainder of this paper. The calculated interval velocity $\mathbf{v}^{obs}(i,d)$, travel time $\mathbf{t}^{obs}(i,d)$, and the thickness of the interval $\mathbf{h}^{obs}(i,d)$ (Figure 2, left) corresponds to the number of the observed reflections $i = 1, \ldots, I$ and the observation days $d = 1, \ldots, D$. The available data consists of 75 GPR observation days that reflect the water content changes for each layer.

[14] To further characterize the plow horizon in the uppermost 0.25 m we introduce the top soil layer by the interval $i = 0$. The wave velocity $\mathbf{v}^{obs}(i = 0,d)$ associated with this layer was taken from the direct ground wave (DGW) traveling through the shallow subsurface [*Galagedara et al.*, 2005a, 2005b]. Since $i = 1$ also includes the DGW interval, this will result in an unequal weighting during the inversion process. Therefore, the interval velocity $\mathbf{v}^{obs}(i=1,d)$, travel time $\mathbf{t}^{obs}(i=1,d)$, and the layer thickness $\mathbf{h}^{obs}(i=1,d)$ of the interval $i = 1$ were recalculated by

$$\mathbf{t}^{obs}(i=1,d)=\frac{\mathbf{h}^{obs}(i=1,d)}{\mathbf{v}^{obs}(i=1,d)}-\frac{\mathbf{h}^{obs}(i=0,d)}{\mathbf{v}^{obs}(i=0,d)} \tag{1}$$

and

$$\mathbf{v}^{obs}(i=1,d)=\frac{\mathbf{h}^{obs}(i=1,d)-\mathbf{h}^{obs}(i=0,d)}{\mathbf{t}^{obs}(i=1,d)}. \tag{2}$$

2.3. Hydrological Model With Film Flow

[15] The water flow simulations (Figure 2, right) were performed using the HYDRUS-1D model [*Šimůnek et al.*, 2008], which solves the one-dimensional Richards equation for variably saturated water flow with

$$\frac{\partial\theta(h)}{\partial t}=\frac{\partial}{\partial z}\left[K(h)\left(\frac{\partial h}{\partial z}+1\right)\right]-S, \tag{3}$$

where $\theta(h)$ is the water content as a function of the pressure head, θ is the volumetric water content (cm^3/cm^3), h is the

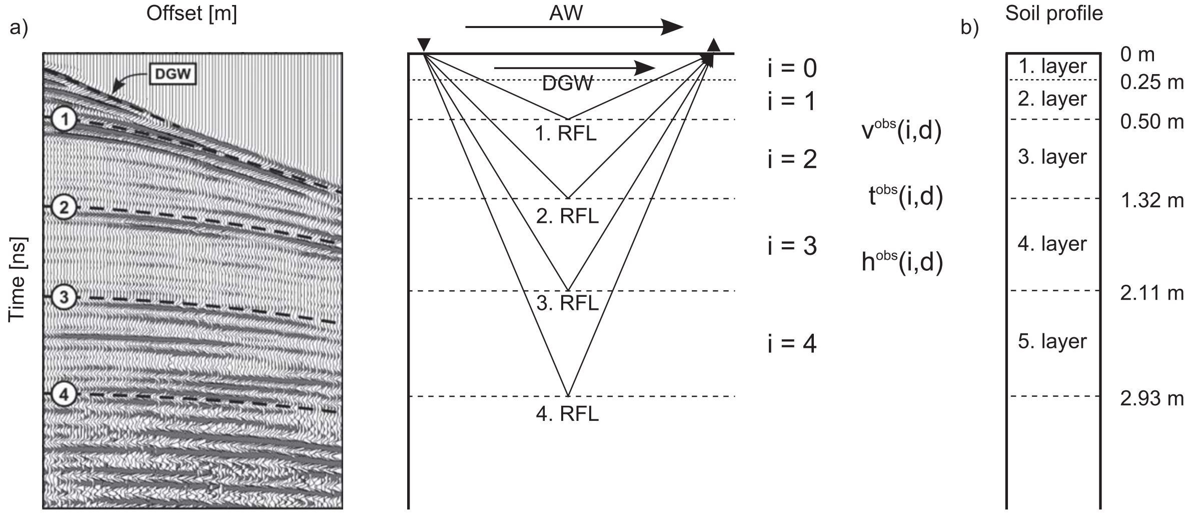

Figure 1. (a) Measured CMP data and model of a layered soil profile obtained from the measured CMP data used for the coupled hydrogeophysical and the corresponding ray-paths of the air-wave (AW), the direct ground-wave (DGW), and the reflections (RFL) in the interval $i = 0, \ldots, I$; (b) corresponding soil profile validated by pitting and coring directly below the survey line after the study period.

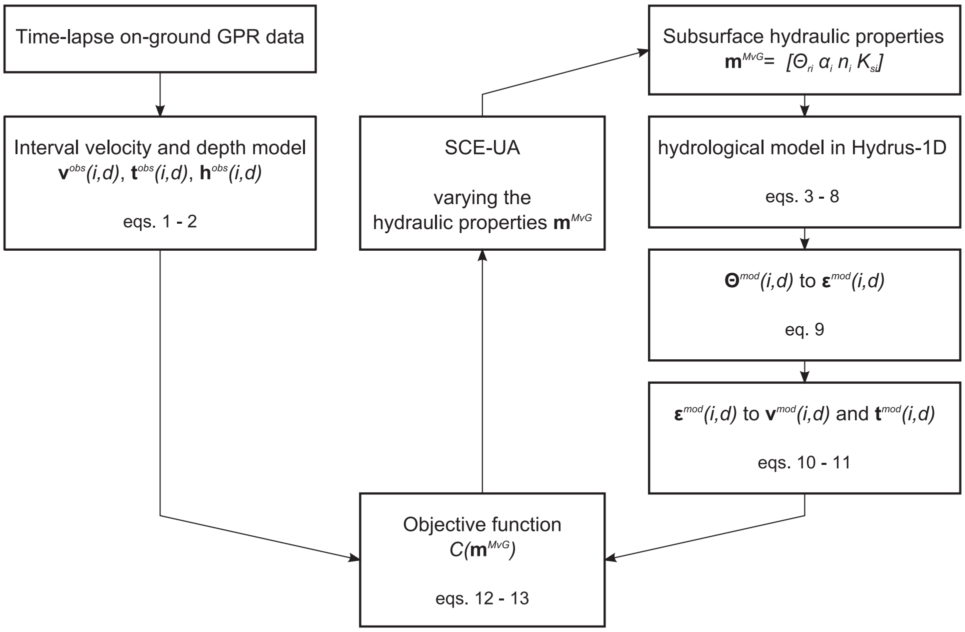

Figure 2. Overview of the coupled hydrogeophysical of time-lapse surface GPR data to estimate the hydraulic properties of a layered subsurface, where θ_{ri} is the residual water content (cm^3/cm^3), α_i (1/cm) and n_i are empirical parameters and K_{si} (cm/d) is the saturated hydraulic conductivity in the interval $i = 0, \ldots, I$.

pressure head (cm), t is the time (d), z is the positive upward spatial component (cm), and $K(h)$ is the hydraulic conductivity (cm/d) as a function of h. The sink term S describes the volume of water removed from a unit volume of soil due to plant water uptake and is defined by the relation of *Feddes et al.* [1974] as

$$S(h)=\alpha_{rwu}(h)S_P, \tag{4}$$

where $\alpha_{rwu}(h)$ is the root water uptake function and S_p is the potential water uptake rate [*Šimůnek et al.*, 2008]. Climatic data were obtained from the University of Waterloo weather station located approximately 7 km east of the test site. Because the plot was covered by short grass, root water uptake was parameterized with the pressure head values $h_0 = -10$ cm below which roots start to extract water from the soil, $h_{opt} = -25$ cm below which roots extract water at the maximum possible rate, $h_{2H} = -200$ cm and $h_{2l} = -800$ cm below which roots cannot longer extract water at the maximum potential transpiration rates $r_{2H} = 0.5$ cm/d and $r_{2L} = 0.1$ cm/d, respectively, and $h_3 = -8000$ cm below which root water uptake ceases. Rooting depth was assigned to reach -15 cm depth, which corresponds to the rooting depth observed at the field plot. The lower boundary was set to free drainage and the overall domain size of 1000 cm was discretized with 1001 equidistant nodes.

[16] The soil water retention function, $\theta(h)$, is described by the Mualem-van Genuchten model [*Mualem*, 1976; *van Genuchten*, 1980]:

$$\theta(h)=\theta_r+\frac{\theta_s-\theta_r}{(1+|\alpha h|^n})^m, \tag{5}$$

where θ_r is the residual water content (cm^3/cm^3), α (1/cm) and n (–) are empirical parameters related to the air entry pressure value and the width of the pore size distribution, respectively, and m is restricted by the Mualem condition to $m = 1 - 1/n$ with $n > 1$. Compared to the Brooks-Corey relationship used by *Steelman et al.* [2012], the Mualem-van Genuchten parameterization offers more degrees of freedom in inverse modeling and is less prone to numerical issues when solving equation (3). The relative unsaturated hydraulic conductivity $K_r^{cap}(h)$ (cm/d) due to capillarity can be calculated as a function of pressure head as follows:

$$K_r^{cap}(h)=\frac{[(1-|\alpha h|^{mn})(1+|\alpha h|^n)^{-m}]^2}{(1+|\alpha h|^n)^{m\lambda}}, \tag{6}$$

where λ is a factor that accounts for pore tortuosity and is set to 0.5. This set of equations is often used to describe capillary fluid flow in a porous media, and allows an appropriate description of the water flow under relatively wet conditions [*van Genuchten*, 1980].

[17] In relatively dry conditions where capillary flow becomes negligible in comparison to film flow, this model parameterization (equation (6)) sometimes fails [*Lenormand*, 1990; *Toledo et al.*, 1990; *Goss and Madliger*, 2007]. To overcome this limitation, we extend equation (6) with a simple empirical approach to describe water flow in films as a function of pressure head with an additional free fitting parameter τ following *Peters and Durner* [2008]:

$$K_r^{film}(h)=[(1+|\alpha h|^n)^{-m}]^\tau. \tag{7}$$

[18] The relative hydraulic conductivity $K_r(h)$ as a function of pressure head can then be described by adding the

contributions of capillary $K_r^{cap}(h)$ and film flow $K_r^{film}(h)$ according to:

$$K_r(h) = (1-\omega)K_r^{cap}(h) + \omega K_r^{film}(h), \tag{8}$$

where ω is the relative contribution of film flow with $0 < \omega < 1$ [*Peters and Durner*, 2008]. For HYDRUS-1D simulations, a layered subsurface is defined in which the Mualem-van Genuchten parameters $\mathbf{m}^{MvG} = [\theta_{ri}, \alpha_i, n_i, K_{si}]$ are prescribed for each interval i. Additionally, the saturated water contents θ_{si} (total porosity) were fixed along the entire profile based on laboratory measurements.

2.4. Conversion of Soil Water Content Into Interval Velocities and Travel Times

[19] To convert the modeled soil water content into interval velocities and travel times, a discrete set of nodes P was selected from the output of the finite element hydrological model to obtain the water content distribution with depth for predefined observation days d. Subsequently, these water content profiles (cm^3/cm^3) were converted into dielectric permittivities using the CRIM model (Figure 2, right) with

$$\sqrt{\boldsymbol{\varepsilon}^{\mathrm{mod}}(i,d)} = \boldsymbol{\theta}^{\mathrm{mod}}(i,d)\sqrt{\varepsilon_w} + (1-\phi)\sqrt{\varepsilon_s} + \left(\phi - \boldsymbol{\theta}^{\mathrm{mod}}(i,d)\right)\sqrt{\varepsilon_a}. \tag{9}$$

with a porosity of $\phi = 0.39$ and the relative permittivities of air $\varepsilon_a = 1$, the solid mineral $\varepsilon_s = 5$, and the water $\varepsilon_w = 84.9$, which corresponds to a temperature of 8°C representing the average annual temperature at the test site. The electromagnetic interval velocities $\mathbf{v}^{mod}(i,d,\mathbf{m}^{MvG})$ and travel time $\mathbf{t}^{mod}(i,d,\mathbf{m}^{MvG})$ are then calculated by:

$$\mathbf{v}^{\mathrm{mod}}\left(i,d,\mathbf{m}^{MvG}\right) = \frac{1}{P_i}\sum_{p_i=1}^{P_i}\frac{v_0}{\sqrt{\boldsymbol{\varepsilon}_{p_i}^{\mathrm{mod}}\left(i,d,\mathbf{m}^{MvG}\right)}} \tag{10}$$

$$\mathbf{t}^{\mathrm{mod}}\left(i,d,\mathbf{m}^{MvG}\right) = \mathbf{h}^{obs}(i,d)\mathbf{v}^{\mathrm{mod}}\left(i,d,\mathbf{m}^{MvG}\right) \tag{11}$$

where $v_0 = 0.2998$ m/ns is the electromagnetic wave velocity in air, $\mathbf{h}^{obs}(i,d)$ is the fixed observed layer thickness, $\boldsymbol{\varepsilon}_{pi}{}^{mod}(i,d,\mathbf{m}^{MvG})$ is the permittivity at node $p_i = 1, \ldots, P_i$ and P_i is the total number of calculation points (Figure 2, right).

2.5. Coupled Inversion for Hydraulic Properties

[20] Using the input parameters $\mathbf{m}^{MvG}$ in the hydrological model, we are now able to calculate GPR interval velocities and travel times (Figure 2, right). Note that, since the interval thickness is fixed and thus the interval velocity and travel directly correlated, both can be used in the objective function. However, since the NMO data were highly variable and the travel time data were very stable over the annual cycle, we evaluate the model fit for a set of input parameters by calculating the misfit between the measured and modeled interval travel times (Figure 2, left) using the objective function (Figure 2, middle):

$$C\left(\mathbf{m}^{MvG}\right) = \frac{1}{D}\sum_{d=1}^{D}\left(\frac{\left|\mathbf{t}^{\mathrm{mod}}(i,d) - \mathbf{t}^{\mathrm{mod}}\left(i,d,\mathbf{m}^{MvG}\right)\right|}{\boldsymbol{\sigma}_t(i)}\right). \tag{12}$$

[21] Here the misfit in the travel times is normalized with the average deviation from the mean interval travel times $\boldsymbol{\sigma}_t(i)$ by:

$$\boldsymbol{\sigma}_t(i) = \frac{1}{D}\sum_{d=1}^{D}\left|t^{obs}(i,d) - \frac{1}{D}\sum_{d=1}^{D}t^{obs}(i,d)\right|. \tag{13}$$

[22] To find the model parameters $\mathbf{m}^{MvG}$ that provide the best fit in the multidimensional solution space, an efficient minimization algorithm must be used (Figure 2, middle). Here we used the shuffled complex evolution (SCE-UA) method described by *Duan et al.* [1992], which is a global optimization routine that combines deterministic and probabilistic approaches to evolve a population of parameter combinations toward the global minimum of the objective function. The coupled inversion was stopped when 10 successive evolution loops did not improve the objective function by >0.01% (Figure 2, middle and right). The corresponding confidence intervals of the inverted model parameters were determined by a first-order approximation as suggested by *Kool and Parker* [1988].

[23] Each soil layer has four unknown parameters, and this increases to six parameters when film flow is considered. Obviously, the computational costs of the inversion process increase significantly when the number of soil layers is increased. In addition, a larger number of soil layers poses larger demands on the information content of the observed data to reliably estimate soil hydraulic parameters. Therefore, we restrict the coupled inversion to two and three-layered soils in the following application to synthetic and measured data.

3. Application to Synthetic Data

[24] To investigate the feasibility of hydraulic parameter estimation by the coupled inversion approach, synthetic time-lapse surface GPR data were modeled for a layered soil. Assuming that the variations in the soil hydraulic parameters for the intervals $i = 1$–4 are negligible, the soil can be described by a two-layered subsurface where a top soil ($i = 0$, Figure 1) is overlying a homogeneous subsoil ($i = 1$–4). For each interval, a total of four hydraulic parameters $\mathbf{m}^{MvG} = [\theta_{ri}, \alpha_i, n_i, K_{si}]$ were defined to simulate water movement through the subsoil (see Table 1).

[25] In addition, by introducing film flow in the uppermost interval $i = 0$ with $\omega = 0.06$ and $\tau = 1.0$ in equations (7) and (8), we explicitly accounted for the contributions of capillary and film flow to the water movement in coarse soils during dry conditions. Here the part of the hydraulic conductivity that is primarily affected by film flow lies in the pressure head range between about $-10^{2.5}$ and -10^4 cm [*Peters and Durner*, 2010].

[26] To test the inversion algorithm and to show how parameter estimation is affected by capillary and film flow, we used two different models where we neglect (*CAP*) and account for film flow (*FILM_CAP*). The simulated water content distributions and interval travel times were obtained by running the models outlined above using the hydraulic parameters obtained from the retention data from *Steelman et al.* [2012]. No noise was added to the simulated interval travel times prior to their use in the coupled

Table 1. Hydraulic Parameter and Objective Functions C for the Two-Layer Inversion of Synthetic Time-Lapse Surface GPR Data Without (*CAP*) and With Film Flow (*FILM_CAP*), Respectively[a]

	MvG Parameter	$\mathbf{m}^{MvG}$ Model	Lower Boundary	Upper Boundary	$\mathbf{m}^{MvG}$ *CAP*	$\mathbf{m}^{MvG}$ *FILM_CAP*
Top soil ($i = 0$)	θ_r (cm^3/cm^3)	0.07	0.04	0.11	0.06 ± 0.004	0.07 ± 0.0001
	α (1/cm)	0.04	0.02	0.06	0.02 ± 0.007	0.04 ± 0.0006
	n	2	1.1	3	2 ± 0.19	2 ± 0.009
	K_s (cm/d)	1140	570	1710	1708 ± 1015	1118 ± 43
	ω	0.06	0	0.1		0.05 ± 0.003
	τ	1	0	5		1.0 ± 0.07
Underlying soil ($i = 1$–4)	θ_r (cm^3/cm^3)	0.06	0.03	0.87	0.06 ± 0.004	0.06 ± 0.0005
	α (1/cm)	0.04	0.02	0.06	0.02 ± 0.0008	0.04 ±0.0006
	n	2	1.1	3	2.2 ± 0.15	2 ± 0.009
	K_s (cm/d)	2600	1300	3900	1304 ± 424	2609 ± 78
Objective function C (equation (12))					0.11	0.0007

[a] The values indicated by ± show the 95% confidence interval based on the first-order approximation.

inversion. The parameter range used in the global optimization is given in Table 1, whereas the saturated water content θ_{si} and the tortuosity factor λ_i were fixed to measured and literature values, respectively. Since more information is contained in the data for the subsoil layer due to reflections from four interfaces as compared to the top soil layer where only the ground wave is used, we reduced the weighting for the lower four reflections by a factor of four such that the information contained in the uppermost layer ($i = 0$) and the remaining layers ($i = 1$–4) are equally weighted when determining the hydraulic parameters of the upper layer and the lower half-space.

[27] Table 1 shows the inversion results for *CAP* and FILM_*CAP* and the corresponding objective function values C. Figure 3 shows the calculated evapotranspiration (black, a) and precipitation (green, a) obtained from the weather data, as well as the simulated average water content profiles (b–f) and the RMSE (in brackets) for the modeled time-lapse GPR data (black) and the inversion results for *CAP* (blue) and *FILM_CAP* (red). Note that the calculated interval velocities (equation (10)) are converted into average water content θ_i along the profile using the CRIM relationship (equation (9)). Although the *CAP* scenario provided a reasonable fit to the GPR data, the inversion seems to compensate for the missing film flow parameters ω and τ by overestimating the wetter and underestimating the dryer events especially within the top layer. As a consequence, the inversion using the *CAP* approach leads to inaccurate hydraulic properties $\mathbf{m}^{MvG}$ (Table 1). In contrast, the predicted water content obtained with the *FILM_CAP* scenario perfectly matched the synthetic data as indicated by the low RMSE and the inverted hydraulic properties were close to the prescribed hydraulic properties (Table 2).

[28] Figure 4 compares the prescribed and inverted pressure-saturation $\theta(h)$ (Figures 4a and 4b) and relative hydraulic conductivity function $K_r(h)$ (Figures 4c and 4d) for the top soil layer and the subsoil. The linear addition of the capillary $K_r^{cap}(h)$ and film flow $K_r^{film}(h)$ for the modeled data (black) and the inversion results *CAP* (blue) and *FILM_CAP* (red) are also illustrated (Figure 4c). It is apparent that $K_r(h)$ is dominated by capillary flow $K_r^{cap}(h)$ in the wet range, whereas in the dry range it is dominated by film flow $K_r^{film}(h)$. In the case of $\theta(h)$, *CAP* returns a different pressure-saturation function for the top layer and the underlying subsoil due to inaccurate values for θ_{ri}, α_i, and n_i, whereas there is a perfect match between the prescribed and inverted pressure-saturation function for *FILM_CAP*. Comparing the inverted hydraulic conductivity function $K_r(h)$ of *CAP* (blue) with the prescribed $K_r^{cap}(h)$ of the modeled data (dashed-dotted black), it is clear that different values for the hydraulic conductivities were obtained for *CAP* for both soil layers. The hydraulic conductivity function $K_r^{cap}(h)$ for the top layer obtained from *FILM_CAP* (dashed red) as well as $K_r(h)$ for the subsoil (d, dashed red) matched perfectly with the prescribed hydraulic conductivity (dashed-dotted black and solid black). Moreover, the inversion results of *FILM_CAP* for $K_r^{film}(h)$ and $K_r(h)$ (dotted and solid red) are in very good agreement with the prescribed function (dashed and solid black) but also show the effect of small inaccuracies in the inverted parameters in $i = 0$. Since film flow primarily affects the hydraulic conductivity for small pressure heads [*Tuller and Or*, 2005; *Vanderborght et al*., 2010], the reason for the inaccuracies in the inversions results might be related to the simulated range of pressure heads that does not reach the low values required for an appropriate parameterization of ω, τ, and K_s.

4. Application to Field Data

[29] To examine the potential of the coupled inversion approach to a field data set, we used the data from *Steelman et al*. [2012] and focused on the period of unfrozen soil between 1 April and 1 November 2008. The overall simulation period in HYDRUS-1D was 214 days where the first 30 days were used as a spin-up to equilibrate the simulated soil water content profile with the atmospheric forcing.

[30] Seasonally persistent reflection events allowed to calculate the interval velocities and travel times of four well-defined stratigraphic interfaces which correspond to the measured GPR intervals $i = 1$–4 (Figure 1). Assuming that the soil below the plow soil can be approximated using a homogeneous hydraulic parameter distribution (Table 3) such that the effects of vertical stratigraphic variations on soil moisture distribution and hydraulic parameters are negligible [*Steelman*, 2012], the inversion of the measured GPR data was carried out for a two-layered subsurface with (*FILM_CAP_L2*) and without film flow (*CAP_L2*) where interval $i = 0$ represents the direct ground wave. We also considered a three-layered subsurface (*FILM_CAP_L3*), where the interval $i = 1$ represents a transition soil layer with a thickness of 25 cm between the top soil and subsoil.

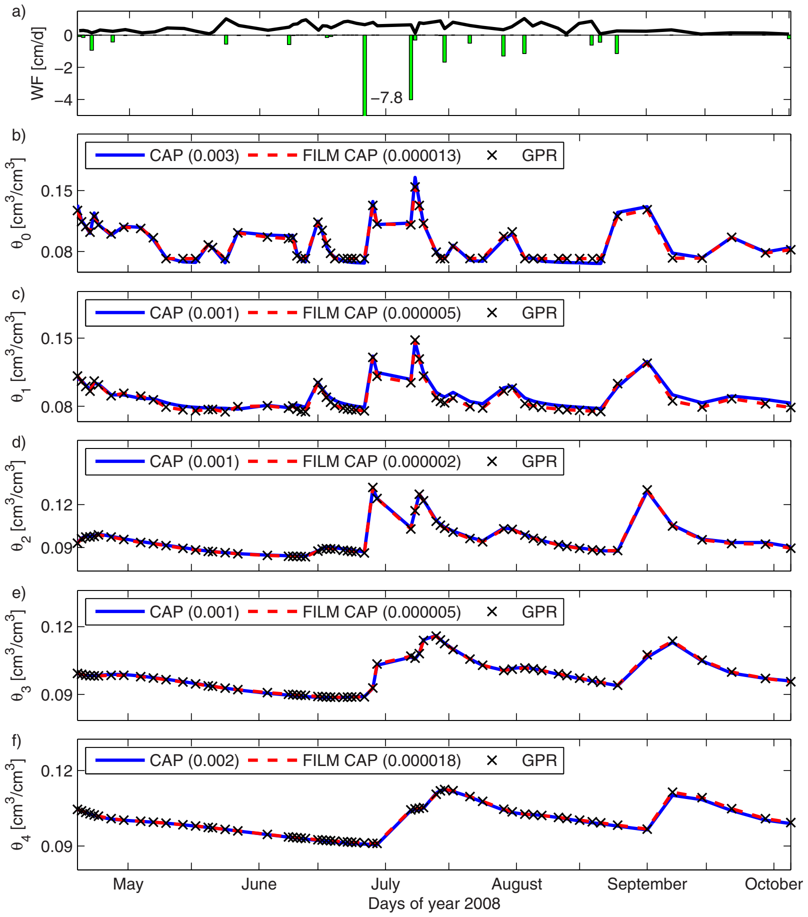

Figure 3. (a) Input evapotranspiration (black) and precipitation (green); (b–f) Average water content profiles and RMSE (brackets) obtained from the modeled time-lapse GPR data with simulated capillary and film flow (black). Blue lines show the results of two-layer inversion *CAP*, red lines indicate the results of *FILM_CAP*. In contrast to *CAP*, in each interval the water content profiles obtained from *FILM_CAP* are overlying with the modeled data. Note that different scales for the axis of the ordinate are used.

[31] Based on the lab-measured retention data of *Steelman et al.* [2012], the corresponding MvG parameters were calculated. Since these MvG model parameters were not estimated based on the GPR measurements, the model run with these parameters is referred to as the uncalibrated model run. Compared to the originally used Brooks-Corey relationship of *Steelman et al.* [2012], the uncalibrated MvG model run describes the GPR measurements well in the wet range but fails for the lower saturations that occurred in the field experiment. The lab-derived MvG parameters were used to define the parameter range for the global optimization as listed in Table 4.

[32] The uncalibrated model run used a two-layered subsurface with an organic-rich plow zone with a thickness of 0.25 m containing the soil roots on top of homogeneous sand extending to a depth of 10 m. A single porosity value of 0.39 was used for the saturated water content θ_{si} along the entire vertical profile, whereas the parameter ranges for θ_{ri}, α_i, n_i

Table 2. RMSE of the Average Water Content θ_i, the Pressure-Saturation Functions $\theta(h)_i$ and Hydraulic Conductivity Functions $K(h)_i$ for the Synthetic Models *CAP* and *FILM_CAP*

		CAP			*FILM_CAP*		
Interval *i*	Depth (m)	$\theta_{i,RMSE}$ (cm^3/cm^3)	$\theta(h)_{i,RMSE}$ (cm^3/cm^3)	$K(h)_{i,RMSE}$ (cm/d)	$\theta_{i,RMSE}$ (cm^3/cm^3)	$\theta(h)_{i,RMSE}$ (cm^3/cm^3)	$K(h)_{i,RMSE}$ (cm/d)
0	0.25	0.003	0.0033	417	0.00001	0.00007	17
1	0.50	0.0008	0.0060	830	0.000005	0.00001	6
2	1.32	0.0006			0.000002		
3	2.11	0.001			0.000005		
4	2.93	0.002			0.00002		

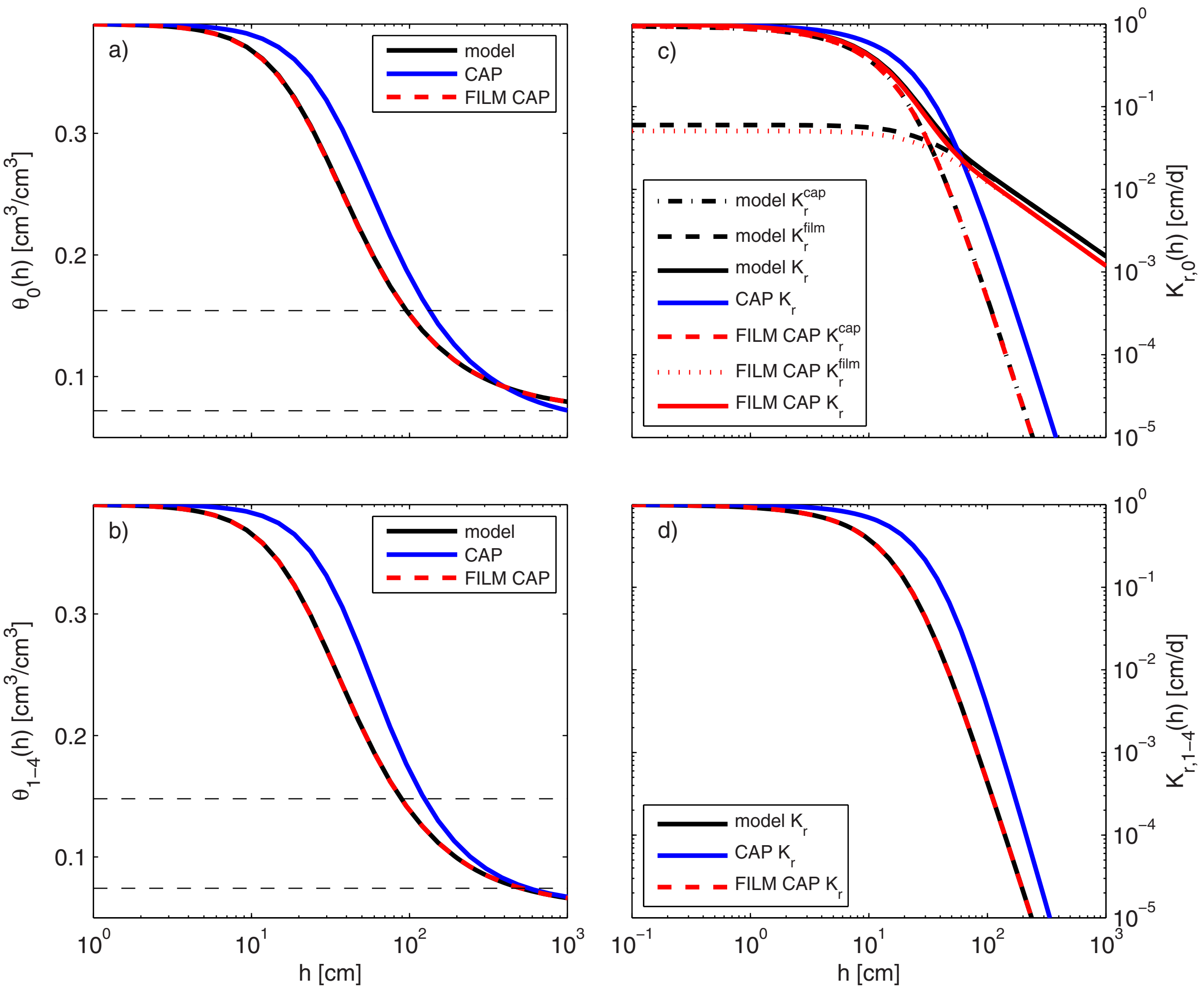

Figure 4. (a, b) Pressure-saturation $\theta(h)$ and (c, d) relative hydraulic conductivity $K_r(h)$ functions based on Mualem-van Genuchten parameterization for the modeled data (black) and, *CAP* (blue) and *FILM_CAP* (red), (a, c) for the ground wave layer and (b, d) the underlying half-space, respectively; (a, c) dashed black lines indicate the range in the water content of the corresponding intervals; (c, d) dashed and dotted lines indicate the relative unsaturated hydraulic conductivity due to capillary $K_r^{cap}(h)$ and film flow $K_r^{film}(h)$, whereas solid lines indicate the relative hydraulic conductivity $K_r(h)$ described as the linear superposition of the contributions of capillary and film flow. From Figure 4c it is obvious that $K_r(h)$ is dominated by capillary flow $K_r^{cap}(h)$ in the wet range, whereas in the dry range it dominated by film flow $K_r^{film}(h)$. A mismatch between the modeled and inverted $K_r^{film}(h)$ clearly shows the effect of small inaccuracies in the inverted parameters in $i = 0$ (see also Table 1). Since film flow primarily affects the hydraulic conductivity for small pressure heads, this misfit might be related to the simulated range of pressure heads that does not reach the low values required for an appropriate parameterization of ω, τ, and K_s. Note that, except $K_r(h)$ in Figure 4c, the calculated retention curves for the modeled data and the inversion results FILM_CAP are overlying.

and K_{si} were wide to avoid excluding plausible parameter values. To obtain an equal weighting of the data in the objective function during the inversion process, we reduced the weighting for the lower four reflections of the two-layer inversions by a factor of four and for the lower three reflections of the three-layer inversions by a factor of three, respectively.

Table 3. Uncalibrated Mualem-van Genuchten Model Calculated From Laboratory Data [*Steelman et al.*, 2012]

Interval i	Depth (m)	θ_r (cm^3/cm^3)	θ_s (cm^3/cm^3)	α (1/cm)	n	K_s (cm/d)	λ
0	0.25	0.07	0.39	0.04	2	1140	0.5
1	0.50	0.06	0.39	0.04	2	2600	0.5
2	1.32	0.06	0.39	0.04	2	2600	0.5
3	2.11	0.06	0.39	0.04	2	2600	0.5
4	2.93	0.06	0.39	0.04	2	2600	0.5

Table 4. Hydraulic Parameter and Objective Function C for the Two-Layer Inversion Without Film Flow (*CAP_L2*) and the Two- (*FILM_ CAP_L2*) and Three-Layer Inversion (*FILM_ CAP_L3*) With Film Flow, Respectively[a]

	MvG Parameter	$\mathbf{m}^{MvG}$ Uncalibrated	Lower Boundary	Upper Boundary	$\mathbf{m}^{MvG}$ *CAP_L2*	$\mathbf{m}^{MvG}$ *FILM_CAP_L2*	$\mathbf{m}^{MvG}$ *FILM_CAP_L3*
Top soil ($i = 0$)	θ_r (cm^3/cm^3)	0.07	0.010	0.14	0.048 ± 0.014	0.053 ± 0.008	0.044 ± 0.008
	α (1/cm)	0.04	0.006	0.08	0.055 ± 0.021	0.050 ± 0.014	0.040 ± 0.010
	n	2	1.1	3	1.6 ± 0.22	1.5 ± 0.1	1.5 ± 0.07
	K_s (cm/d)	1140	171	11404	1291 ± 1030	5780 ± 2031	7352 ± 1914
	ω	0.	0	0.1		0.03 ± 0.01	0.03 ± 0.008
	τ	0	0	3		1.2 ± 0.6	0.6 ± 0.2
Transition zone ($i = 1$)	θ_r (cm^3/cm^3)	0.06	0.009	0.12			0.080 ± 0.005
	α (1/cm)	0.04	0.006	0.08			0.016 ± 0.006
	n	2	1.1	3			2.6 ± 0.5
	K_s (cm/d)	2600	390	26006			13721 ± 3309
Underlying soil ($i = 2$–4)	θ_r (cm^3/cm^3)	0.06	0.009	0.12	0.054 ± 0.014[b]	0.054 ± 0.008[b]	0.047 ± 0.011
	α (1/cm)	0.04	0.006	0.08	0.025 ± 0.005[b]	0.023 ± 0.008[b]	0.015 ± 0.003
	n	2	1.1	3	2.5 ± 0.9[b]	2.4 ± 0.4[b]	2.2 ± 0.3
	K_s (cm/d)	2600	390	26006	10933 ± 7729[b]	16080 ± 4602[b]	14440 ± 2661
Objective function C (equation (12))					0.76	0.79	0.72

[a] The values indicated by ± show the 95% confidence interval based on the first-order approximation.

[b] For the two-layer inversion the transition zone and the underlying soil are combined to a half-space.

[33] Table 4 shows the optimized hydraulic parameters and the minimum objective function C for all considered scenarios. *CAP_L2* and *FILM_CAP_L2* only showed small differences in the hydraulic properties and the objective function values. With the exception of saturated hydraulic conductivity K_s, which exhibited a larger uncertainty based on the *Kool and Parker* [1988] approximation, these inversions return comparable hydraulic properties for the subsurface. In the case of *FILM_CAP_L3*, the inverted hydraulic parameters for $i = 0$ and $i = 2$–4 are close to the results of *CAP_L2* and *FILM_CAP_L2*. The film flow parameter ω and τ obtained from *FILM_CAP_L2* and *FILM_CAP_L3* are in very good agreement but the additional transition zone $i = 1$ in *FILM_CAP_L3* clearly leads to a further decrease in the overall misfit to the measured data (Table 4).

[34] Figure 5 shows the average water content profiles obtained from the time-lapse GPR data (black crosses), the uncalibrated model (black) and *CAP_L2* (blue), *FILM_-CAP_L2* (red) and *FILM_CAP_L3* (green). Figure 6 shows the calculated interval velocities and travel times and the corresponding RMSE for each interval is presented in Table 5. Note that the interval velocities and travel times in Figure 6 are calculated based on the average water content; hence they show the same characteristic in the data fitting and the RMSE.

[35] Since the measurement period was characterized by numerous large precipitation events, greater water content variability near the surface with numerous drainage pulses propagate through the soil profile [*Steelman et al.*, 2012]. While wetter periods in the uppermost subsurface were well described by the inversion results, measurements from dryer periods were not described as well. Here *FILM_CAP_L2* shows a slightly better fit in the interval $i = 0$–1 (Figure 5). Although the dynamic water content changes obtained from the inversion results are in good agreement, particularly for the intervals $i = 2$–4, the differences between the two and three-layer inversion with film flow are small. The additional film flow parameter in *FILM_CAP_L2* did not improve the inversion results and the three-layered model in *FILM_CAP_L3* only slightly improved the inversion result (see Table 4). This behavior is also indicated in Figure 7, which shows a weak positive correlation between the water content calculated from the measured GPR data using the CRIM model and the predicted water content from the hydraulic parameters determined from the uncalibrated model (black), *CAP_L2* (blue), *FILM_CAP_L2* (red) and *FILM_CAP_L3* (green) for the intervals $i = 0$ and $i = 2$–4, respectively. Within (a) the top soil layer and (b) the subsoil, *CAP_L2*, *FILM_CAP_L2* and *FILM_CAP_L3* return reliable values for θ_0 and $\theta_{2\text{–}4}$ and lie close to the dashed black 1:1 line, whereas the uncalibrated model (solid black) clearly overestimates the water content inferred from the measured GPR data and does not lie on the dashed black 1:1 line. The uncalibrated model resulted in R^2 values of 0.52 and 0.36 for intervals $i = 0$, and $i = 2$–4, respectively, whereas the inversion results show R^2 values of 0.54–0.57 and 0.43–0.47, respectively. Note that the larger objective function obtained for the *FILM_CAP_L2* inversion as shown in Table 4 is due to a decreased fit in the lower intervals $i = 2$–4 as shown in Figure 7b.

[36] To illustrate the reliability of the inversion results, Figure 8 compares the volumetric water content obtained from *CAP_L2* (blue), *FILM_CAP_L2* (red) and *FILM_CAP_L3* (green) as a function of the pressure head with discrete laboratory measurements of the hydraulic parameters, carried out on soil samples from 0.2, 0.4, 0.5, 0.6, 0.8, 1.0, 1.3, and 1.6 m depth (black), respectively. Compared to the predictions based on hydraulic parameters derived from the laboratory data at 0.2 m, the inversion results return higher values for the air entry pressure α and lower values for the pore size distribution n, resulting in flatter retention curves for the top soil layer (Figure 8a). For interval $i = 1$ (Figure 8b) and $i = 2$–4 (Figure 8c) especially the predicted water content for *CAP_L2* gives a good fit to the laboratory data. However, considering that the field conditions are almost exclusively at very low water contents ($i = 1$–4), the inversion of the data predicts a reasonable curve for a sand. Note that the porosity value of 0.39 used in the inversion of the

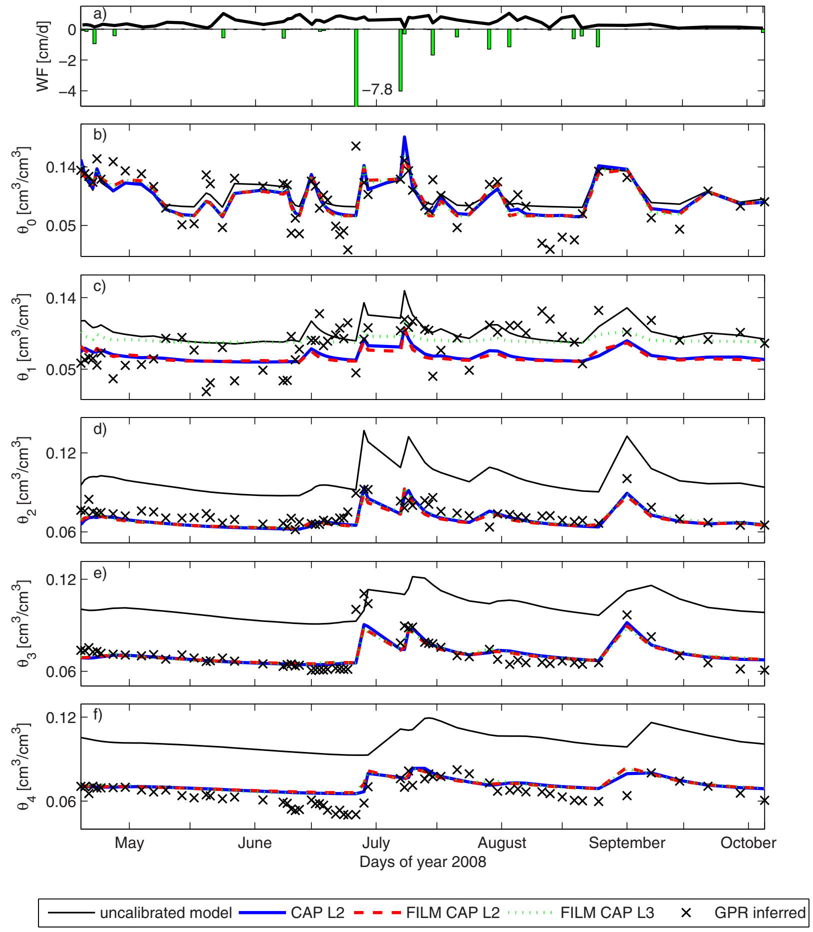

Figure 5. (a) Measured evapotranspiration (black) and precipitation (green); (b–f) Water content profiles obtained from the time-lapse GPR data (black crosses), the uncalibrated model (black) and the inversion results for *CAP_L2* (blue), *FILM_CAP_L2* (red), and *FILM_CAP_L3* (green), respectively. Except interval $i = 1$, the results of *CAP_L2*, *FILM_CAP_L2*, and *FILM_CAP_L3* are overlying and in good agreement with the water content obtained from the GPR measurements. Especially for the intervals $i = 2$–4 the inversion result show a significant improved data fit. Note that different scales for the axis of the ordinate are used.

data is based on intact bulk density samples taken from the field. The systematically lower values from the laboratory data (0.35–0.37) probably reflect the effects of repacking.

[37] Figure 9 shows saturated hydraulic conductivity K_s obtained from the laboratory data, *CAP_L2* (blue), *FILM_CAP_L2* (red), and *FILM_CAP_L3* (green). Due to different soil samples at the depths 0.6, 0.8, 1.0, 1.3, and 1.6 m, the laboratory data return a range of values for saturated hydraulic conductivity in the interval $i = 2$–4. Although the saturated hydraulic conductivity values predicted by *CAP_L2*, *FILM_CAP_L2*, and *FILM_CAP_L3* are significantly higher, the inversion results show a similar trend as the laboratory data.

5. Discussion

[38] Inversion of the field GPR data provided hydraulic conductivity functions that indicated a higher fitted hydraulic conductivity than expected from corresponding laboratory data. This is very commonly found because of the scale dependence of hydraulic conductivity that consistently shows that the small volume of laboratory soil samples leads to lower hydraulic conductivity values than field hydraulic conductivity estimates with a larger volume [e.g., *Rovey and Cherkauer*, 1995]. This difference in hydraulic conductivity also explains the offsets between water content obtained from the uncalibrated model run and the water contents predicted by the hydraulic parameters estimated from the GPR measurements.

[39] In the analysis of the field data, neither the consideration of film flow nor the implementation of a transition zone between the topsoil and subsoil improved the inversion results substantially compared to the simple inversion based on a two-layer subsurface only. There are a variety of reasons that could be responsible for the remaining mismatches between modeled and GPR estimated water contents. To assure reliable parameter estimates from model inversion, the hydrological model should describe the dominating processes present in the measured data in detail. In the case of an inaccurate hydrological model, the coupled

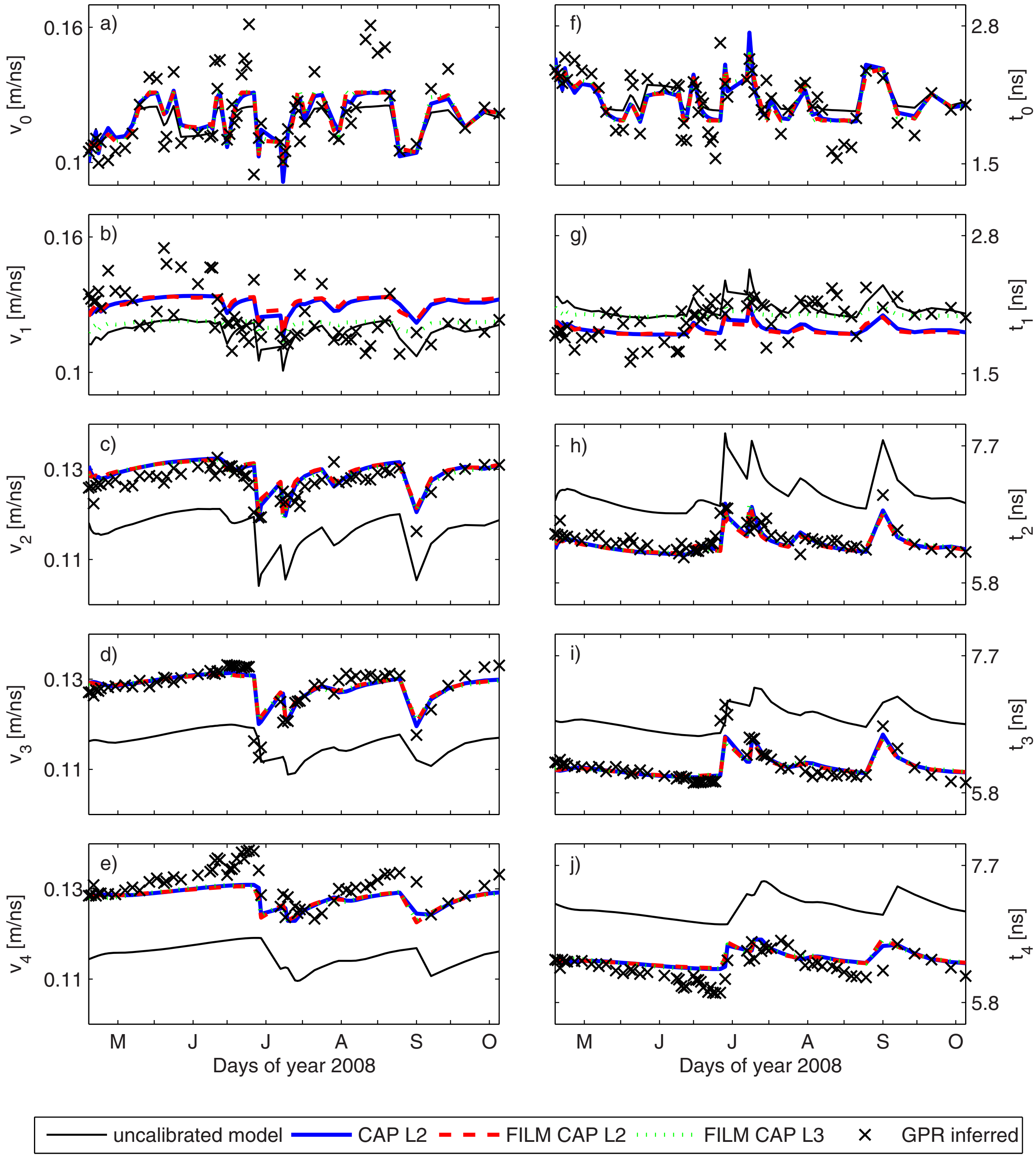

Figure 6. Observed (a–e) GPR interval velocities (black crosses) and (g–j) travel times and calculated interval velocities and travel times for the uncalibrated model (solid black line), *CAP_L2* (blue), *FILM_CAP_L2* (red), and *FILM_CAP_L3* (green), respectively. Note that different scales for the axis of the ordinate are used.

inversion will optimize the model parameters to achieve the best possible data fit. As a consequence, the inversion may return inaccurate hydraulic properties, as was observed in the synthetic case study. In the following, we discuss three unresolved uncertainties in the conceptualization, parameterization, and implementation of the hydrological model used in our study.

[40] First of all, there is considerable uncertainty in the parameterization of root water uptake models because of the use of empirical model parameters and the need to provide a typically unknown root length distribution with depth. In addition, root water uptake processes are only rudimentary described in our and most other 1-D hydrological models [e.g., *Javaux et al.*, 2008]. Recently, a more advanced approach to describe root water uptake has been proposed for such models [*Couvreur et al.*, 2012], which may alleviate some of the reported uncertainties in future studies.

Table 5. RMSE of the Calculated Water Content θ_i, the Interval Velocity v_i and Travel Time t_i Based on *CAP_L2*, *FILM_CAP_L2*, and *FILM_CAP_L3*, Respectively

Interval *i*	$\theta_{i,\mathrm{RMSE}}$ (cm^3/cm^3)	$v_{i,\mathrm{RMSE}}$ (m/ns)	$t_{i,\mathrm{RMSE}}$ (ns)
Uncalibrated Model			
0	0.032	0.013	0.19
1	0.031	0.013	0.20
2	0.029	0.011	0.65
3	0.029	0.013	0.67
4	0.033	0.016	0.83
CAP_L2			
0	0.011	0.011	0.18
1	0.008	0.011	0.18
2	0.009	0.003	0.13
3	0.006	0.003	0.15
4	0.010	0.004	0.16
FILM_CAP_L2			
0	0.010	0.011	0.17
1	0.006	0.012	0.19
2	0.008	0.003	0.14
3	0.004	0.003	0.14
4	0.013	0.004	0.17
FILM_CAP_L3			
0	0.018	0.011	0.17
1	0.014	0.012	0.17
2	0.013	0.003	0.13
3	0.011	0.003	0.15
4	0.019	0.004	0.17

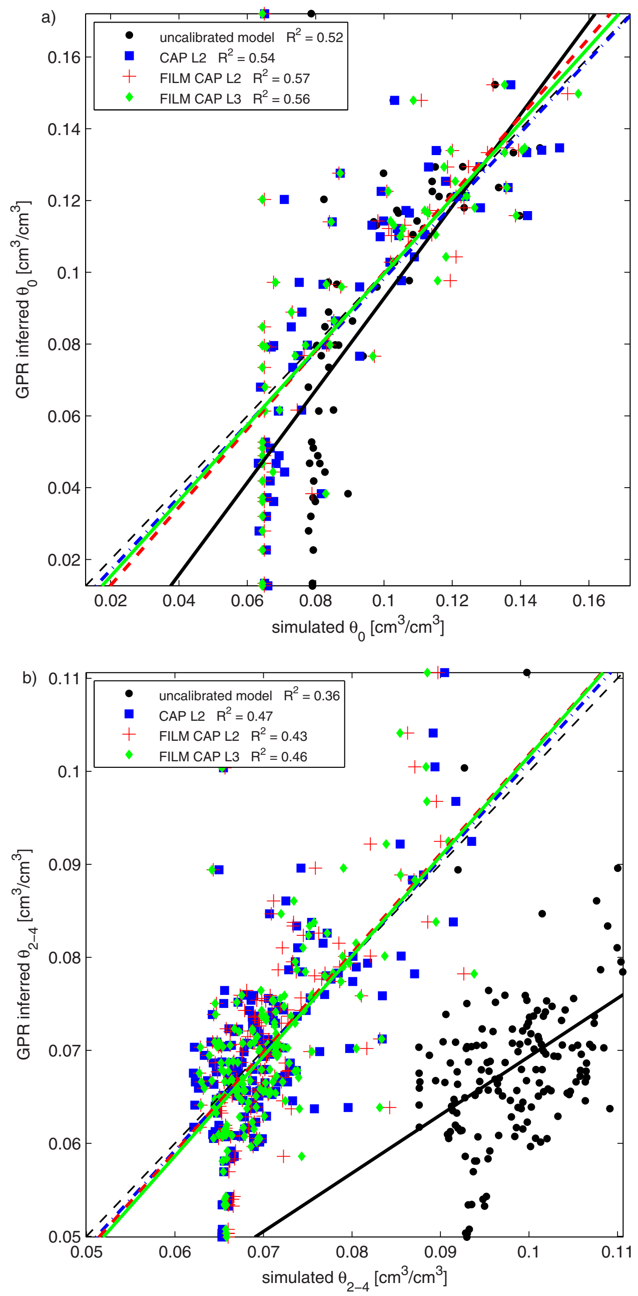

Figure 7. Correlation between the water content inferred from GPR measurements (dashed black) and the water content obtained from the uncalibrated model (black), and from *CAP_L2* (blue), *FILM_CAP_L2* (red), and *FILM_CAP_L3* (green), for the intervals (a) $i = 0$ and (b) $i = 2$–4, respectively.

[41] Second, the modeling approach of *Peters and Durner* [2008] that was used here in an attempt to increase evaporation in dry soil conditions by allowing for film flow is not well founded in theory [*Shokri and Or*, 2010; *Peters and Durner*, 2010]. As described above, inaccurate process descriptions may lead to inappropriate inversion results. More advanced models that describe coupled vapor, heat, and water transport are available [*Saito et al.*, 2006; *Steenpass et al.*, 2010], and the use of such models in coupled inversion of GPR data as proposed by *Moghadas et al.* [2013] warrants further investigation.

[42] Figure 10 shows the calculated cumulative evapotranspiration, evaporation and transpiration for the scenarios with (*FILM_CAP_L2*, *FILM_CAP_L3*) and without film flow (*CAP*). It can be seen that the model conceptualization without film flow resulted in considerably lower evaporation and somewhat higher transpiration so that total water loss by evapotranspiration was lower in the case that film flow was not considered. These simulation results suggest that actual evapotranspiration obtained by lysimeter or micrometeorological measurements may be useful to discriminate between competing model conceptualizations. However, such measurements are not available for the test site used in this study.

[43] Finally, the inversion results obviously also depend on the use of appropriate boundary conditions, especially for atmospheric forcing. Unfortunately, no weather station was available at the test site and climatic data had to be used from the weather station in Waterloo, which is approximately 7 km east of the test site. Figure 11 shows the high regional variability in rainfall using two additional weather stations in Elora (25 km north of the test site) and Stratford (40 km east of the test site). This high regional variability illustrates the considerable uncertainty in the meteorological boundary conditions at the test site (especially for the timing and intensity of convective storm events). Any deviation between the actual and prescribed meteorological conditions potentially influences the presented inversion results.

6. Conclusions

[44] A coupled inversion scheme that combines conventional ray-based analysis of time-lapse surface GPR data with a hydrological forward model was presented and

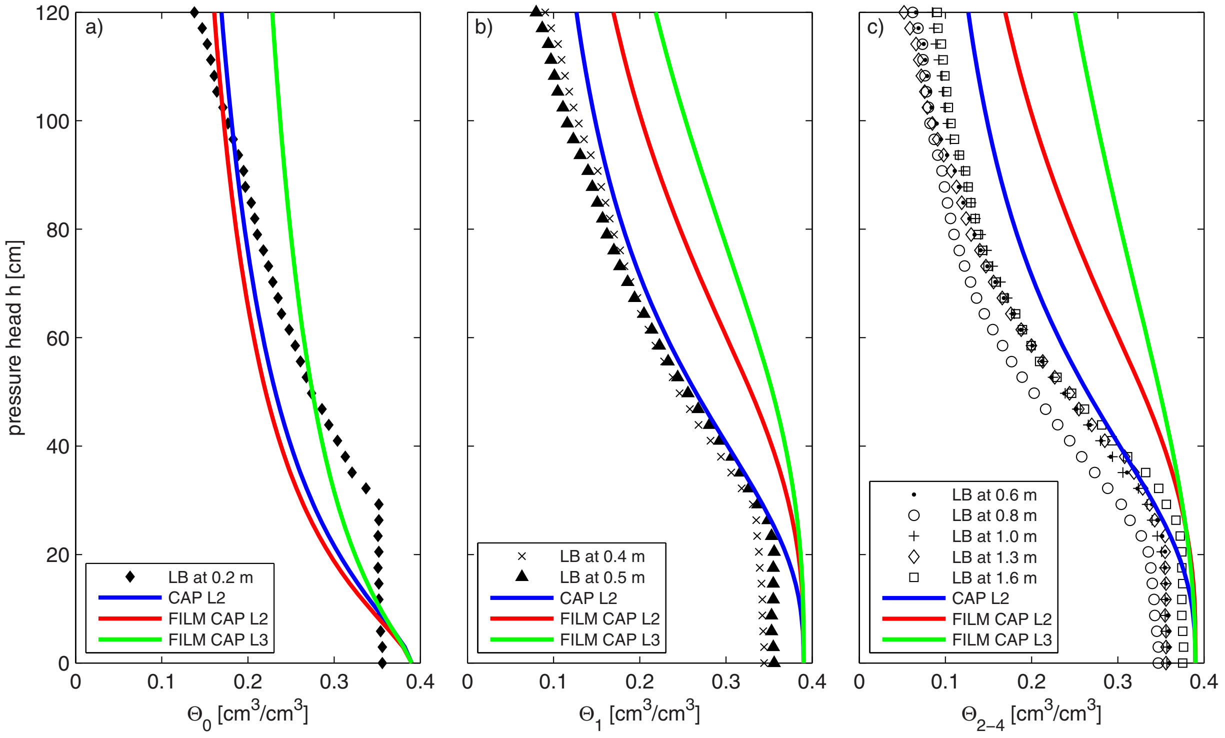

Figure 8. Volumetric water content obtained from *CAP_L2* (blue), *FILM_CAP_L2* (red), *FILM_CAP_L3* (green), and discrete laboratory measurements (LB) on soil samples from 0.2, 0.4, 0.5, 0.6, 0.8, 1.0, 1.3, and 1.6 m depth (black) for (a) the ground wave layer ($i = 0$), (b) the transitions zone ($i = 1$), and (c) the underlying half-space ($i = 2–4$). Dashed black lines indicate the range in the water content of the corresponding intervals.

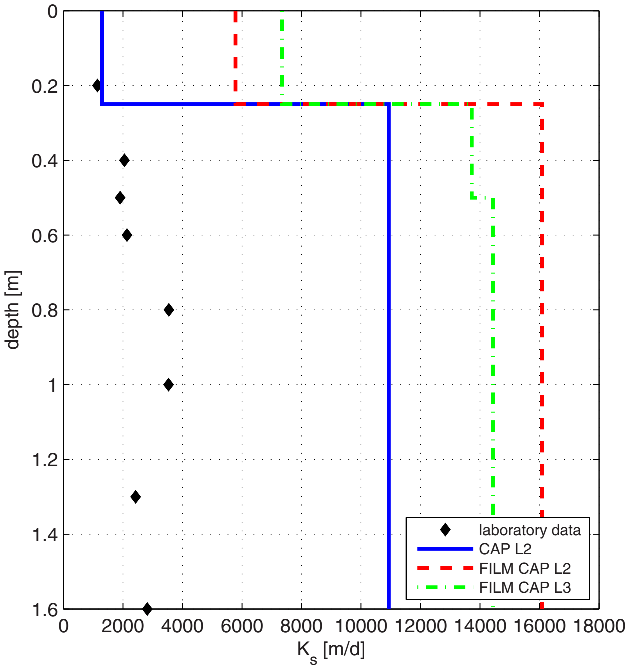

Figure 9. Saturated hydraulic conductivity K_s obtained from *CAP_L2* (blue), *FILM_CAP_L2* (red), *FILM_CAP_L3* (green), and laboratory data at the at the depths 0.2, 0.5, 0.6, 0.8, 1.0, 1.3, and 1.6 m (black). Although the K_s values predicted by *CAP_L2*, *FILM_CAP_L2*, and *FILM_CAP_L3* are significantly higher, the inversion results show a similar trend as the laboratory data.

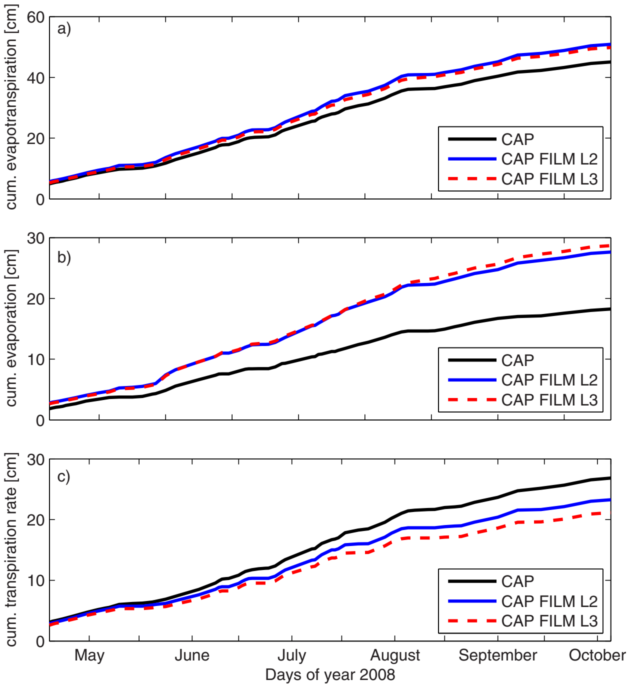

Figure 10. Cumulative (a) evapotranspiration, (b) evaporation, and (c) transpiration rate obtained from the hydrological forward model in HYDRUS-1D for *CAP* (black), *CAP_FILM_L2* (blue), and *CAP_FILM_L3* (dashed red). Compared to *CAP_FILM_L2* and *CAP_FILM_L3*, neglecting film flow *CAP* seems to underestimate the evaporation of the soil.

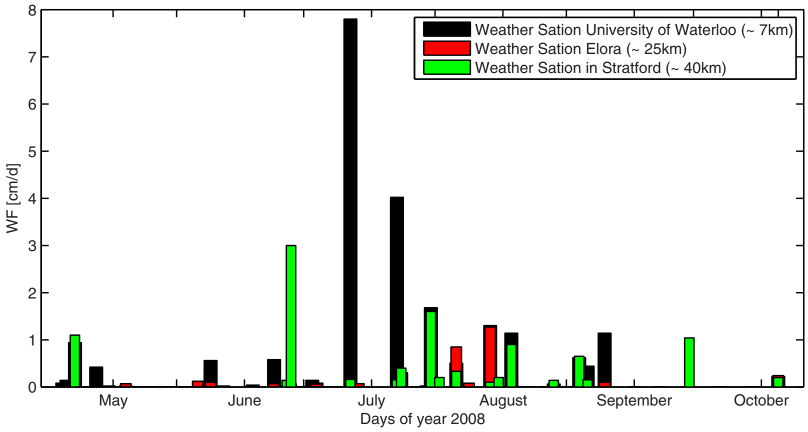

Figure 11. Variability in the rainfall recorded at weather station of the University of Waterloo approximately 7 km east of the test site (black), as well as at the weather stations in Elora (red) and Straford (green) 25 km north and 40 km east of the test site, respectively.

applied to synthetic and measured GPR data over a horizontally layered subsurface. To allow an appropriate description of the water flow under wet and dry conditions, we explicitly account for capillary and film flow in the uppermost subsurface layer.

[45] In case of synthetic data with film flow, the coupled inversion approach that did not consider film flow was able to reproduce modeled data despite a wrong model formulation and returned different hydraulic parameters that partly compensated the error introduced by neglecting film flow. The modeled data were correctly inverted using the coupled inversion approach that included film flow. Here our results clearly show the importance of an appropriate model conceptualization when using coupled inversion.

[46] In the case of measured time-lapse GPR data, we used a two and three-layered subsurface. The inversion was able to reduce the RMSE between measured and predicted soil water content as compared to an uncalibrated model relying on laboratory-derived hydraulic parameters. Here especially the RMSE of the subsoil could be improved and the increase in soil water content in response to rainfall events could be described very well. The remaining mismatches between measured and modeled data were attributed to uncertainty in (i) model conceptualization and parameterization associated with root water uptake, (ii) appropriate representation of evaporation processes, and (iii) meteorological conditions at the research site.

[47] In this study, coupled inversion relied on standard ray-based techniques to analyze time-lapse surface GPR data. Although more data were available that also included frozen soil [*Steelman et al.*, 2012], we focus on the period of unfrozen soil since a conventional dispersion inversion [*van der Kruk et al.*, 2009; *Steelman et al.*, 2010], needed to extract the medium properties from dispersive GPR data due to freezing and thawing, could not be included in the current inversion.

[48] Following developments for off-ground GPR [e.g., *Lambot et al.*, 2006a, 2006b, 2009; *Jadoon et al.*, 2012], it is certainly promising to extend the coupled inversion approach presented here with the recently developed full-waveform inversion (FWI) for surface GPR [*Busch et al.*, 2012, 2013]. Such a full-waveform inversion can probably better deal with dispersive data due to freezing and thawing waveguides and the challenges occurring when interference from wetting fronts and the aggregation of water at soil boundaries are present, as discussed by *Mangel et al.* [2012]. Compared to full-waveform inversion of off-ground GPR, such inversion of surface GPR data may lead to improved characterization of multilayered soils to a larger soil depth because of the higher penetration depth of surface GPR.

[49] **Acknowledgments.** We thank Steven Moysey and two anonymous reviewers for their detailed reviews that significantly improved the manuscript. We thank the Jülich Supercomputing Center (JSC) for providing access to the JUROPA high-performance cluster.

References

Bauer, J., L. Weihermüller, J. A. Huisman, M. Herbst, A. Graf, J. M. Sequaris, and H. Vereecken (2012), Inverse determination of heterotrophic soil respiration response to temperature and water content under field conditions, *Biogeochemistry*, *108*, 119–134.

Bayer, A., H.-J. Vogel, O. Ippisch, and K. Roth (2005), Do effective properties for unsaturated weakly layered porous media exist? An experimental study, *Hydrol. Earth Syst. Sci.*, *9*, 517–522.

Behaegel, M., P. Sailhac, and G. Marquis (2007), On the use of surface and ground temperature data to recover soil water content information, *J. Appl. Geophys.*, *62*, 234–243.

Brooks, R. H., and A. T. Corey (1966), Properties of porous media affecting fluid flow, *J. Irrig. Drain. Div.*, *72*(IR2), 61–88.

Busch, S., J. van der Kruk, J. Bikowski, and H. Vereecken (2012), Quantitative conductivity and permittivity estimation using full-waveform inversion of on-ground GPR data, *Geophysics*, *77*, H79–H91.

Busch, S., J. van der Kruk, and H. Vereecken (2013), Improved characterization of fine texture soils using on-ground GPR full-waveform inversion, *IEEE Trans. Geosci. Remote Sens.*, doi:10.1109/TGRS.2013.2278297, in press

Couvreur, V., J. Vanderborght, and M. Javaux (2012), A simple three-dimensional macroscopic root water uptake model based on the hydraulic architecture approach, *Hydrol. Earth Syst. Sci.*, *16*, 2957–2971, doi: 10.5194/hess-16–2957-2012.

Duan, Q. Y., S. Sorooshian, and V. Gupta (1992), Effective and efficient global optimization for conceptual rainfall-runoff models, *Water Resour. Res.*, *28*, 1015–1031.

Ersahin, S., and A. R. Brohi (2006), Spatial variation of soil water content in topsoil and subsoil of a Typic Ustifluvent, *Agric. Water Manage.*, *83*, 79–86.

Feddes, R. A., E. Bresler, and S. P. Neuman (1974), Field test of a modified numerical model for water uptake by root systems, *Water Resour. Res.*, *10*, 1199–1206.

Galagedara, L. W., G. W. Parkin, J. D. Redman, P. von Bertoldi, and A. L. Endres (2005a), Field studies of the GPR ground wave method for estimating soil water content during irrigation and drainage, *J. Hydrol.*, *301*, 182–197.

Galagedara, L. W., J. D. Redman, G. W. Parkin, A. P. Annan, and A. L. Endres (2005b), Numerical modeling of GPR to determine the direct ground wave sampling depth, *Vadose Zone J.*, *4*, 1096–1106.

Goss, K.-U., and M. Madliger (2007), Estimation of water transport based on in situ measurements of relative humidity and temperature in a dry Tanzanian soil, *Water Resour. Res.*, *43*, W05433, doi:10.1029/2006WR005197.

Hinnell, A. C., T. P. A. Ferré, J. A. Vrugt, J. A. Huisman, S. Moysey, J. Rings, and M. B. Kowalsky (2010), Improved extraction of hydrologic information from geophysical data through coupled hydrogeophysical inversion, *Water Resour. Res.*, *46*, W00D40, doi:10.1029/2008WR007060.

Huisman, J. A., S. S. Hubbard, J. D. Redman, and A. P. Annan (2003), Measuring soil water content with ground penetrating radar: A review, *Vadose Zone J.*, *2*, 476–491.

Jadoon, K. Z., L. Weihermüller, B. Scharnagl, M. B. Kowalsky, M. Bechtold, S. S. Hubbard, H. Vereecken, and S. Lambot (2012), Estimation of soil hydraulic parameters in the field by integrated hydrogeophysical inversion of time-lapse Ground-Penetrating Radar data, *Vadose Zone J.*, *11*(4), 279–295, doi:10.2136/vzj2011.0177.

Javaux, M., T. Schroeder, J. Vanderborght, and H. Vereecken (2008), Use of a three-dimensional detailed modelling approach for predicting root water uptake, *Vadose Zone J.*, *7*, 1079–1088, doi:10.2136/vzj2007.0115.

Kool, J. B., and J. C. Parker (1988), Analysis of the inverse problem for transient unsaturated soil water flow, *Water Resour. Res.*, *24*, 817–830.

Kowalsky, M. B., S. Finsterle, J. Peterson, S. Hubbard, Y. Rubin, E. Majer, A. Ward, and G. Gee (2005), Estimation of field-scale soil hydraulic and dielectric parameters through joint inversion of GPR and hydrological data, *Water Resour. Res.*, *41*, W11425, doi:10.1029/2005WR004237.

Lambot, S., E. C. Slob, I. van den Bosch, B. Stockbroeckx, and M. Vanclooster (2004), Modeling of ground-penetrating radar for accurate characterization of subsurface electric properties, *IEEE Trans. Geosci. Remote Sens.*, *42*, 2555–2568.

Lambot, S., E. C. Slob, M. Vanclooster, and H. Vereecken (2006a), Closed loop GPR data inversion for soil hydraulic and electric property determination, *Geophys. Res. Lett.*, *33*, L21405, doi:10.1029/2006GL027906.

Lambot, S., M. Antoine, M. Vanclooster, and E. C. Slob (2006b), Effect of soil roughness on the inversion of off-ground monostatic GPR signal for noninvasive quantification of soil properties, *Water Resour. Res.*, *42*, W03403, doi:10.1029/2005WR004416.

Lambot, S., E. C. Slob, J. Rhebergen, O. Lopera, K. Z. Jadoon, and H. Vereecken (2009), Remote estimation of the hydraulic properties of a sand using full-waveform integrated hydrogeophysical inversion of time lapse, off-ground GPR data, *Vadose Zone J.*, *8*, 743–754.

Lenormand, R. (1990), Liquids in porous media, *J. Phys. Condensed Matter*, *2*, SA79–SA88.

Looms, M. C., A. Binley, K. H. Jensen, L. Nielsen, and T. M. Hansen (2008), Identifying unsaturated hydraulic parameters using an integrated data fusion approach on cross-borehole geophysical data, *Vadose Zone J.*, *7*, 238–248.

Mangel, A. R., S. M. J. Moysey, J. C. Ryan, and J. A. Tarbutton (2012), Multi-offset ground-penetrating radar imaging of a lab-scale infiltration test, *Hydrol. Earth Syst. Sci.*, *16*, 4009–4022.

Mboh, C. M., J. A., Huisman, and H. Vereecken (2011), Feasibility of sequential and coupled inversion of time domain reflectometry data to infer soil hydraulic parameters under falling head infiltration, *Soil Sci. Soc. Am. J.*, *75*, 775–786.

Mertens, J., H. Madsen, K. Kristensen, D. Jaques, and J. Feyen (2005), Sensitivity of soil parameters in unsaturated zone modelling and the relation between effective, laboratory and in situ estimates, *Hydrol. Processes*, *19*, 1611–1633.

Moghadas, D., K. Z. Jadoon, J. Vanderborght, S. Lambot, and H. Vereecken (2013), Effects of near surface soil moisture profiles during evaporation on far-field ground-penetrating radar data: A numerical study, *Vadose Zone J.*, *12*(2), 1–11, doi:10.2136/vzj2012.0138.

Moysey, S. M. J. (2010), Hydrologic trajectories in transient ground-penetrating radar reflection data, *Geophysics*, *75*(4), WA211–WA219.

Mualem, Y. (1976), A new model for predicting the hydraulic of unsaturated porous media, *Water Resour. Res.*, *12*, 513–522.

Peters, A., and W. Durner (2008), A simple model for describing hydraulic conductivity in unsaturated porous media accounting for film and capillary flow, *Water Resour. Res.*, *44*, W11417, doi:10.1029/2008WR007136.

Peters, A., and W. Durner (2010), Comment on ‘‘A simple model for describing hydraulic conductivity in unsaturated porous media accounting for film and capillary flow’’ by N. Shokri and D. Or, *Water Resour. Res.*, *46*, W06802, doi:10.1029/2010WR009181.

Rovey, C. W., and D. S. Cherkauer (1995), Scale dependence of hydraulic conductivity measurements, *Ground Water*, *33*(5), 769–780, doi:10.1111/j.1745–6584.1995.tb00023.x.

Rucker, D., and P. A. Ferré (2004), Parameter estimation for soil hydraulic properties using zero-offset borehole radar: Analytical method, *Soil Sci. Soc. Am. J.*, *68*, 1560–1567.

Saito, H., J. Šimůnek, and B. P. Mohanty (2006), Numerical analysis of coupled water, vapor, and heat transport in the vadose zone, *Vadose Zone J.*, *5*(2), 784–800, doi:10.2136/vzj2006.0007.

Shokri, N., and D. Or (2010), Comment on ‘‘A simple model for describing hydraulic conductivity in unsaturated porous media accounting for film and capillary flow’’ by A. Peters and W. Durner, *Water Resour. Res.*, *46*, W06801, doi:10.1029/2009WR008917.

Šimůnek, J., M. T. van Genuchten, and M. Sejna (2008), Development and applications of the HYDRUS and STANMOD software packages and related codes, *Vadose Zone J.*, *7*, 587–600.

Steelman, C. M. (2012), Evaluating vadose zone moisture dynamics using ground-penetrating radar, Ph.D. thesis, Univ. of Waterloo, Waterloo, ON.

Steelman, C. M., A. L. Endres, and J. van der Kruk (2010), Field observations of shallow freeze and thaw processes using high-frequency ground-penetrating radar, *Hydrol. Processes*, *24*, 2022–2033.

Steelman, C. M., A. L. Endres, and J. P. Jones (2012), High-resolution ground-penetrating radar monitoring of soil moisture dynamics: Field results, interpretation, and comparison with unsaturated flow model, *Water Resour. Res.*, *48*, W09538, doi:10.1029/2011WR011414.

Steenpass, C., J. Vanderborght, M. Herbst, J. Šimůnek, and H. Vereecken (2010), Estimating soil hydraulic properties from infrared measurements of soil surface temperatures and TDR data, *Vadose Zone J.*, *9*(4), 910–924, doi:10.2136/vzj2009.0176.

Toledo, P., R. Novy, H. Davis, and L. Scriven (1990), Hydraulic conductivity of porous media at low water content, *Soil Sci. Soc. Am. J.*, *54*, 673–679.

Topp, G. C., J. L. Davis, and A. P. Annan (1980), Electromagnetic determination of soil water content: Measurements in coaxial transmission lines, *Water Resour. Res.*, *16*, 574–582.

Tuller, M., and D. Or (2005), Water films and scaling of soil characteristic curves at low water contents, *Water Resour. Res.*, *41*, W09403, doi:10.1029/2005WR004142.

Vanderborght, J., A. Graf, C. Steenpass, B. Scharnagl, N. Prolingheuer, M. Herbst, H. J. H. Franssen, and H. Vereecken (2010), Within-field variability of bare soil evaporation derived from eddy covariance measurements, *Vadose Zone J.*, *9*, 943–954.

van der Kruk, J., C. M. Steelman, A. L. Endres, and H. Vereecken (2009), Dispersion inversion of electromagnetic pulse propagation within freezing and thawing soil waveguides, *Geophys. Res. Lett.*, *36*, L18503, doi:10.1029/2009GL039581.

van Genuchten, M. T. (1980), A closed-form equation for predicting the hydraulic conductivity of unsaturated soils, *Soil Sci. Soc. Am. J.*, *44*, 892–898.

Weihermüller, L., J. A. Huisman, A. Graf, M. Herbst, and J. M. Sequaris (2009), Multistep outflow experiments to determine soil physical and carbon dioxide production parameters, *Vadose Zone J.*, *8*, 772–782.

Wharton, R. P., G. A. Hazen, R. N. Rau, and D. L. Best (1980), Electromagnetic propagation logging: Advances in technique and interpretation, paper SPE 9267, SPE Annual Technical Conference and Exhibition, 21–24 September, Dallas, Tex.